Tractography From HARDI Using an Intrinsic Unscented Kalman Filter

Guang Cheng, Hesamoddin Salehian, John R. Forder, and Baba C. Vemuri*

***Abstract*—A novel adaptation of the unscented Kalman filter (UKF) was recently introduced in literature for simultaneous multitensor estimation and fiber tractography from diffusion MRI. This technique has the advantage over other tractography methods in terms of computational efficiency, due to the fact that the UKF simultaneously estimates the diffusion tensors and propagates the most consistent direction to track along. This UKF and its variants reported later in literature however are not intrinsic to the space of diffusion tensors. Lack of this key property can possibly lead to inaccuracies in the multitensor estimation as well as in the tractography. In this paper, we propose a novel intrinsic unscented Kalman filter (IUKF) in the space of diffusion tensors which are symmetric positive definite matrices, that can be used for simultaneous recursive estimation of multitensors and propagation of directional information for use in fiber tractography from diffusion weighted MR data. In addition to being more accurate, IUKF retains all the advantages of UKF mentioned above. We demonstrate the accuracy and effectiveness of the proposed method via experiments publicly available phantom data from the fiber cup-challenge (MICCAI 2009) and diffusion weighted MR scans acquired from human brains and rat spinal cords.**

***Index Terms*—Intrinsic Kalman filtering, diffusion MRI, diffusion tensor estimation, tractography.**

I. Introduction

DIFFUSION weighted magnetic resonance imaging (DWMRI) is a relatively nascent MRI technique that allows one to infer neuronal pathways in the central nervous systems. Several algorithms have been reported in literature to reconstruct the nerve fiber bundles from DWMRI scans of the brain, spinal cord and other parts of the anatomy. The process of tracing the neuronal fibers is called tractography. Tractography techniques in literature fall in two primary categories: deterministic and probabilistic.

The streamline algorithm is one of the most popular deterministic tractography technique. Given the DWMR signal at each voxel, streamline methods are applied post reconstruction of either the diffusion tensor, the fiber orientation distribution function (fODF) or the ensemble average propagator (EAP) function [1]–[7]. Depending on the model used to describe the fiber orientations, several streamline-based methods have been introduced. In diffusion tensor imaging (DTI) where the DWMR signal decay is modeled by a monoexponential function characterized by a zero mean Gaussian distribution, which is fully represented by a second order diffusion tensor [1], the streamline follows the direction of the largest eigenvector of the diffusion tensor. As alternatives to streamline applied to DTI, tensor deflection (TEND) methods were developed in [8] where at each voxel, the entire DT is used as a linear operator to deflect the incoming vector direction, as opposed to only following the largest eigenvector, leading to smoother tract reconstruction.

It is now well known that DTI can not capture the complex local fiber geometries occurring in the presence of multiple fibers in a voxel, e.g., crossing fibers. To address this shortcoming, higher order tensors have been used to capture the diffusivity function profile [9]–[12]. However, it is well known that the maxima of the diffusivity profile do not correspond to the fiber orientations [13]. Nevertheless, they do capture the geometry of the diffusivity and allow one to compute several useful anisotropy properties [13]. If however, the higher order tensors are used to represent the EAP, then, standard streamline methods are applicable to the directions representing their maxima for tractography. Further investigation to capture the fiber orientations in the presence of multiple fibers at a voxel resulted in various streamline methods based on tracing the vector field of maxima of orientation distribution functions (ODFs) [14], [15] and weighted mixture models [5], [16] extracted from high angular resolution diffusion imaging (HARDI) or from Q-ball imaging data [17].

Front-propagation approaches are another group of deterministic tractography, where some approaches have treated the white matter bundles as a Riemannian manifold, equipped with a metric inferred from the diffusion tensors [18], [19]. The tractography problem is then reduced to computation of geodesic curves using this metric. While robust, these methods are based on DTI and effectively are inadequate in dealing with multifiber geometry present at voxels.

Presence of noise during DWMR data acquisition process, as well as the deficiency of the diffusion model used to reconstruct the DWMR signal, leads to inevitable uncertainties in the estimated fiber orientation at each voxel [20]. Probabilistic tractography is a class of tracking methods that were introduced to take such uncertainties into account. In these algorithms, a population of different fiber tracts emanating from a specific

Manuscript received June 30, 2014; accepted August 17, 2014. Date of publication September 05, 2014; date of current version December 24, 2014. This research was supported in part by the National Institutes of Health under Grant NS066340 to B. C. Vemuri. *Asterisk indicates corresponding author.*

G. Cheng and H. Salehian are with the Department of Computer and Information Science and Engineering (CISE), University of Florida, Gainesville, FL 32611 USA (e-mail: gcheng@cise.ufl.edu; salehian@cise.ufl.edu).

J. R. Forder is with the Department of Radiology, University of Florida, Gainesville, FL 32611 USA (e-mail: jforder@mbi.ufl.edu).

*B. C. Vemuri is with the Department of Computer and Information Science and Engineering (CISE), University of Florida, Gainesville, FL 32611 USA (e-mail: vemuri@cise.ufl.edu).

Color versions of one or more of the figures in this paper are available online at http://ieeexplore.ieee.org.

Digital Object Identifier 10.1109/TMI.2014.2355138

seed point are reconstructed. The probability for each pathway is estimated based on local probability functions defined at voxels along the path. These algorithms fall into two general categories. The methods in the first group, are the so called parametric methods which estimate the noise parameters using some probability distribution. Several parametric methods were reported in literature that were mostly based on single tensor [20], [21], multitensor [22], [23] or Q-ball imaging [24]. On the other hand, the techniques in the second category use residual bootstrap as a nonparametric statistical procedure to estimate the uncertainty in the DWMR signal reconstruction. Various residual bootstrap methods were proposed depending on the model being used, including DTI [25], [26], q-ball ODF [27] and Constrained Spherical Deconvolution [28]. In [29], authors augmented the residual bootstrap technique with a curve inference labeling technique to identify voxels containing single, crossing or fanning fibers, leading to detailed subvoxel geometry information. Probabilistic methods resort to the full spherical function representing the diffusion ODF profile—as opposed to using only the principal directions—which however is usually not indicative of the fiber orientations. To overcome this issue, Descoteaux *et al.* [30] developed a method to transform the diffusion ODF into a fiber ODF using what is known as the deconvolution sharpening transform. Probabilistic methods however in general are far more computationally expensive than the deterministic counter parts. Thus, in this work, we will limit ourselves to a deterministic method such as the streamline method.

Most of the aforementioned streamline tractography methods are based on a two stage procedure: i) estimation of the underlying model from DWMR signal over the whole image, ii) tracking based on the estimated model in i). Some how, no possible interaction between these stages has been exploited until, authors in [31] proposed a clever multitensor tractography method based on the Unscented Kalman Filter (UKF) [32]. The UKF-based method in [31] enjoys the important advantage of *simultaneous multitensor reconstruction and propagation of most consistent directional information for use in tractography*. This advantage is evident in two aspects namely: 1) The regularized tensor reconstruction is only performed along the estimated fibers, which yields significant computational efficiency, since one only needs to reconstruct multitensors at the voxels that are likely on fiber paths, and not all over the image; 2) propagating the most consistent direction to track along achieves smoothness of the tracts being traced using a streamline technique. The streamline method implicitly regularizes the tracts by using the most consistent direction from the smooth estimates of tensors obtained from the UKF.

Various types of UKF-based tractography methods have been reported in literature [31], [33], [34]. In [31] a weighted mixture model is used to reconstruct the signal at each voxel. The state vector is then formed by one principal eigenvector and two largest eigenvalues for each component. In this state model it was assumed that diffusion tensors have ellipsoidal shapes, i.e., $\lambda_1 \gg \lambda_2 = \lambda_3$, where λ_i's are the eigenvalues. This assumption causes inaccuracies in reconstruction of the underlying signal, as the information carried by the smallest eigenvalue, λ_3, is not taken into account. Finally, in [34] authors proposed an extension of UKF to HARDI data modeled by ODFs. However, none of the mixture model-based UKF techniques described above are intrinsic to the space of diffusion tensors, possibly resulting in nonpositive definite diffusion tensors that lead to inaccuracies in the reconstruction as well as fiber tracking. Although, later versions [35] did overcome some of these deficiencies via nonintrinsic computationally expensive methods. In general it would be more apt to track the full tensor and naturally enforce the positivity constraint resorting to the intrinsic geometry of the space of diffusion tensors.

It is well known that diffusion tensors lie in the space of symmetric positive definite (SPD) matrices denoted by P_n, which is not a Euclidean space but a Riemannian manifold [36]. Hence, algorithms that are based on vector operations can not be applied directly to this space, and nontrivial extensions are needed. Some extensions of UKF to various Riemannian manifolds have been reported in literature. Recently, a generalization of the UKF to Riemannian manifolds was presented in [37]. This extension is quite general, but has some technical issues that were not carefully considered. Further, no applications to tractography were considered, which is the main driving application in this paper.

In this paper, we propose a novel intrinsic UKF on P_n and provide examples for the $n = 3$ case. A preliminary version of this work (four pages long) was presented in [38]. This paper is a significant extension providing the detailed theory and an extensive set of experiments testing the theory. We apply this filter to the publicly available fiber cup challenge DWMRI phantom data [39], and real DWMRI datasets from rat spinal cords and human brains respectively. In both real and synthetic data cases, we consider only single shell DWMRI scans. The accuracy of our tractography results on the fiber cup data are better than other methods published in literature with respect to the spatial distance measure used for tractography evaluation in [39], and are competitive with regards other error measures used in the fiber cup challenge [39]. Additionally, we have made the MATLAB implementation of this method publicly available at http://www.nitrc.org/projects/iukf_2013.

The rest of the paper is organized as follows: the intrinsic unscented Kalman filter (IUKF) is described in Section II, where, in Section II-B the basic geometric properties are briefly introduced, followed by a novel dynamic model defined for the multitensor model. We then present the IUKF algorithm and finally the experiments are presented in Section III and conclusions drawn in Section IV.

II. Intrinsic Unscented Kalman Filter for Diffusion Tensors

In this section, we will first provide motivation for the use of a dynamic stochastic filter such as the Kalman filter for the tractography task. Then, we briefly describe its extension to the UKF followed by a detailed description of our IUKF to estimate diffusion tensors which lie in the space of $n \times n$ SPD matrices denoted by P_n and propagate directional information that facilitate tractography. Prior to describing the IUKF, we will however give some mathematical preliminaries involving a brief introduction of Riemannian geometry on P_n and refer the readers to [36] for further details on Riemannian geometry.

A. A Stochastic Dynamic Filter

As described earlier, tractography involves tracing out the most likely direction of nerve fiber bundles in the given DWMR data. However, it is nontrivial to estimate the fiber bundle direction from the DWMR data. This is why most of the fiber analysis frameworks [14]–[16], [18], [19] contain an estimation stage to denoise and estimate the EAP, ODF, etc., and the fiber tracking is dependent on these estimated results. One drawback for such an analysis framework is that in the estimation stage, the smoothness along the fiber bundles is not considered because the location of these fiber bundles are not known during this estimation. One way out is to estimate the EAP (or fODF) recursively along the fiber, so the fiber tracking and estimation can be done simultaneously. An extra bonus of this new framework is that we now only need to do the estimation at the voxels along the fiber, which would reduce the computational complexity.

Taking a closer look, we can find that by viewing the tensors as the state and MR signal as the observation, the EAP estimation along the fiber would nicely fit into a state-space model (see Section II-C), where the smoothness constraint can be enforced recursively along the fiber. Thus, the problem of tensor estimation and tracking is apt for the application of a recursive stochastic dynamic filter such as the well known Kalman filter (KF). Several such methods were reviewed in Section I. The KF is a linear filter and its extension called the extended KF (EKF) is its nonlinear version wherein, the probability distribution of the system state is approximated by a Gaussian random variable and propagated through the system dynamics analytically by using a first-order linearization of the nonlinear system. It has been shown that this can lead to large errors in the posterior estimates of the mean and covariance of the transformed Gaussian random variable and at times lead to divergence of the filter [32]. A stable and accurate solution to this problem is achieved by the UKF. This is done by careful selection of sample points to estimate the mean and covariance of the Gaussian random variable representing the system state and when propagated through the system dynamics, captures the mean and covariance of the transformed Gaussian random variable accurately to the third order. Since, in the tractography problem, we model the diffusion MR signal by a mixture model in the presence of intravoxel heterogeneity and we want to simultaneously estimate the model parameters and propagate the most consistent directional information to facilitate tractography, the UKF is better suited for this problem than the KF.

Now that we have laid out the motivation for using the UKF for our problem at hand, we are still faced with one crucial issue, the parameters we want to estimate are matrix-variate random variables which are diffusion tensors (SPD matrices). Thus the standard UKF is unsuitable since it expects inputs to be in a vector space and SPD matrices belong to a Riemannian manifold with negative sectional curvature [36]. We are now ready to present the background Riemannian geometry of the space of SPD matrices and then the modified UKF that we dub, the intrinsic UKF or simply IUKF.

B. Riemannian Geometry on p_n

The space of $n \times n$ SPD matrices, known as P_n, is a smooth manifold and a symmetric space [36] and is obtained by quotienting out the group of orthogonal matrices from the general linear group, i.e., $P_n = GL(n)/O(n)$ where $GL(n)$ denotes the General Linear group (the group of $n \times n$ nonsingular matrices) and $O(n)$ denotes the space of $n \times n$ orthogonal matrices. Let $\mathbf{X} \in P_n, \mathbf{g} \in GL(n)$, the group action $\mathbf{g}$ applied to $\mathbf{X}$ is given by $\mathbf{X}[\mathbf{g}] = \mathbf{g}\mathbf{X}\mathbf{g}^t$. It is known that $GL(n)$ acts transitively on P_n, i.e., $\forall \mathbf{X}, \mathbf{Y} \in P_n, \exists \mathbf{g} \in GL(n)$ such that $\mathbf{X}[\mathbf{g}] = \mathbf{Y}$.

At each point $\mathbf{X} \in P_n$ the tangent space is denoted by $T_{\mathbf{X}}P_n$, which can be identified with a vector space $Sym(n)$—the space of $n \times n$ symmetric matrices. For tangent vectors $\mathbf{U}$ and $\mathbf{V} \in T_{\mathbf{X}}P_n$ the canonical inner-product/metric is defined as $< \mathbf{U}, \mathbf{V} >_{\mathbf{X}} = tr(\mathbf{X}^{-1/2}\mathbf{U}\mathbf{X}^{-1}\mathbf{V}\mathbf{X}^{-1/2})$. It is easy to verify that this metric is invariant to GL actions, i.e., $< \mathbf{U}, \mathbf{V} >_{\mathbf{X}} = < \mathbf{g}\mathbf{U}\mathbf{g}^t, \mathbf{g}\mathbf{V}\mathbf{g}^t >^t_{\mathbf{g}\mathbf{X}\mathbf{g}}$. Given the metric, the distance between any two points $\mathbf{X}, \mathbf{Y} \in P_n$ can be defined as the geodesic length between any two points $\mathbf{X}, \mathbf{Y}$ on the manifold. On P_n this distance can be computed in a closed form as, $dist(\mathbf{X}, \mathbf{Y})^2 = tr(\log^2(\mathbf{X}^{-1}\mathbf{Y}))$, where, $\log$ is the matrix log function. The exponential map denoted by $\mathrm{Exp}_{\mathbf{X}}(\cdot)$ at a certain point $\mathbf{X} \in P_n$ maps a tangent vector $\mathbf{V} \in T_{\mathbf{X}}P_n$ rooted at the origin to a geodesic in the manifold. That is, the curve segment $\gamma(t) = \mathrm{Exp}_{\mathbf{X}}(t\mathbf{V}), t \in [0, 1]$ is a geodesic from $\gamma(0) = \mathbf{X}$ to $\mathrm{Exp}_{\mathbf{X}}(\mathbf{V})$. The Log map ($Log_{\mathbf{X}}(\cdot)$) is the inverse of the Exponential map. The Exponential and Log maps on P_n are given by $\mathrm{Exp}_{\mathbf{X}}(\mathbf{V}) = \mathbf{X}^{1/2}\exp(\mathbf{X}^{-1/2}\mathbf{V}\mathbf{X}^{-1/2})\mathbf{X}^{1/2}$, and $\mathrm{Log}_{\mathbf{X}}(\mathbf{Y}) = \mathbf{X}^{1/2}\log(\mathbf{X}^{-1/2}\mathbf{Y}\mathbf{X}^{-1/2})\mathbf{X}^{1/2}$, where $\mathbf{X}, \mathbf{Y} \in P_n, \mathbf{V} \in T_{\mathbf{X}}P_n$, and Log and Exp denote the matrix $\exp$ and $\log$ operators. Many operations in Euclidean space can be applied to P_n by first Log mapping points on the manifold to the tangent space and mapping back to P_n (using the exponential map) after the operation.

The generalization of the arithmetic mean in the Euclidean space to the Riemannian manifold is the Karcher mean—an estimator that minimizes the sum of squared geodesic distances. In P_n the Karcher mean of set of elements $\mathbf{X}_i \in P_n$ is given by, $\boldsymbol{\mu}^* = \widehat{\sum}_i \mathbf{X}_i = \mathrm{argmin}_{\boldsymbol{\mu}} \sum_i dist^2(\mathbf{X}_i, \boldsymbol{\mu})$, which can be computed using a gradient descent technique.

For a certain matrix-valued random variable $\mathbf{X} \in P_n$, the intrinsic expectation can be defined similarly to the Karcher mean $E(\mathbf{X}) = \mathrm{argmin}_{\mathbf{Y}} \int_{P_n} dist^2(\mathbf{X}, \mathbf{Y}) dP(X)$, where $dP(X)$ is the probability measure. This expectation is called the Karcher expectation. The matrix-valued random variable $\mathbf{X}$ can then be projected to $T_{E(\mathbf{X})}P_n$, and the covariance matrix can be defined in this tangent space.

C. The State Transition and Observation Models

We are now ready to present the details of the IUKF. Prior to delving into the details though, it suffices to say that to construct the UKF, one needs to specify three models: 1) a prior model, to describe the system state prior to making any measurements; 2) a measurement (observation) model, which relates measurements to the current state; and 3) the state-transition model, which describes the evolution of the current state over time. These three models are used to describe the evolution of the current state of the stochastic system and its relationship to the measurements. To obtain the optimal estimate of the current state of the system, the UKF operates in two phases namely, the extrapolation phase which predicts the next state (given the previous best estimate of the same) and the covariance associated with this predicted state. The second phase is the correction phase which updates the predictions with the observations. IUKF also operates within this general framework except, various operations within the filter are based on P_n and not in a vector space. We now present the various modules of the IUKF.

1) Observation Model: In this paper, we use the bi-tensor diffusion model as was done in [31], where the DWMR signal is represented by the sum of two Gaussian functions

$$S^{(n)} = S_0(e^{-b_n \mathbf{g}_n^t \mathbf{D}^{(1)} \mathbf{g}_n^t} + e^{-b_n \mathbf{g}_n^t \mathbf{D}^{(2)} \mathbf{g}_n^t}) + r_n \qquad (1)$$

where $\mathbf{D}^{(i)} \in P_n$ is the ith (3×3) diffusion tensor, $\mathbf{g}_n$ denote the direction of nth magnetic gradient, and b is the corresponding b-value, $S^{(n)}$ is the MR signal along the nth gradient direction, and r_n is the additive Gaussian noise. Note that the concentration tensor/matrix is the inverse covariance matrix of a Gaussian. Instead of the weighted sum, we use direct sum of two Gaussian functions, because the weight can be integrated into the diffusion tensor $\mathbf{D}^{(i)}$

$$\begin{aligned} w_i e^{-b_n \mathbf{g}_n^t \tilde{\mathbf{D}}^{(i)} \mathbf{g}_n^t} &= e^{-b_n \mathbf{g}_n^t (\tilde{\mathbf{D}}^{(i)} - log(w_i)/b_n \mathbf{I}) \mathbf{g}_n^t} \\ &= e^{-b_n \mathbf{g}_n^t \mathbf{D}^{(i)} \mathbf{g}_n^t} \end{aligned} \qquad (2)$$

where $\tilde{\mathbf{D}}^{(i)}$ is the diffusion tensor under the weighted sum model and w_i is the ith weight. Since $w_i \leq 1$, we can guarantee that $\mathbf{D}^{(i)}$ is always positive definite. From (2) we can see that when using a constant b value, as in high angular resolution diffusion imaging (HARDI), there is insufficient data to resolve the degrees of freedom of both weights and diffusion tensors respectively. So instead, we use the direct sum model as in (1) which reduces the number of parameters (the estimation of the weight of each component is not need) in the system, and thus reduces the computational load and makes the system more stable. However, the direct sum model and the weighted sum model are not geometrically equivalent because $w_i = 0$ is mapped to infinity in the direct sum model.

2) State Transition Model: Here we would like to estimate diffusion tensors $\mathbf{D}^{(1)}, \mathbf{D}^{(2)} \in P_n$ along each fiber, which leads to an estimation problem on P_n. The state transition model on P_n in this paper is based on the GL operation and the LogNormal distribution [40] and is given by

$$\begin{aligned} \mathbf{D}_{k+1}^{(1)} &= \mathrm{Exp}_{\mathbf{F}\mathbf{D}_k^{(1)}\mathbf{F}^t}(\mathbf{v}_k^{(1)}) \\ \mathbf{D}_{k+1}^{(2)} &= \mathrm{Exp}_{\mathbf{F}\mathbf{D}_k^{(2)}\mathbf{F}^t}(\mathbf{v}_k^{(2)}) \end{aligned} \qquad (3)$$

where, $\mathbf{D}_k^{(1)}, \mathbf{D}_k^{(2)}$ are the two tensor-valued states at step k, $\mathbf{F}$ is the state transition matrix (a GL operation), $\mathbf{v}_k^{(1)}$ and $\mathbf{v}_k^{(2)}$ are the Gaussian distributed random symmetric matrices representing the state transition noise for $\mathbf{D}_k^{(1)}$ and $\mathbf{D}_k^{(2)}$ in the tangent space $T_{\mathbf{F}\mathbf{D}_k^{(1)}\mathbf{F}^t}P_3$ and $T_{\mathbf{F}\mathbf{D}_k^{(2)}\mathbf{F}^t}P_3$, respectively. Note that P_n here is P_3 since $n = 3$ for our problem.

Here we assume that the two state transition noise models are independent from each other and the previous states. The covariance matrices of the two state transition noise models are $\mathbf{Q}_k^{(1)}$ and $\mathbf{Q}_k^{(2)}$ respectively. The covariance matrix $\mathbf{Q}_k^{(i)}$ $i = 1, 2$ is a 6× 6 matrix defined for the tangent vectors in $T_{\mathbf{F}\mathbf{D}_k^{(i)}\mathbf{F}^t}P_3$. Note that $\mathbf{Q}_k^{(i)}$ is not invariant to GL transforms on P_n. Let $\mathbf{X} = \mathrm{Exp}_{\boldsymbol{\mu}}(\mathbf{v}) \in P_n$ be a matrix-variate random variable, where $\mathbf{v}$ is a random vector drawn from a zero mean Gaussian with $\mathbf{Q}$ being the covariance matrix. Then, after a GL transform $\mathbf{g} \in GL(n)$, the new random variable $\mathbf{Y} = \mathbf{g}\mathbf{X}\mathbf{g}^t = \mathrm{Exp}_{\mathbf{g}\boldsymbol{\mu}\mathbf{g}^t}(\mathbf{u})$. The covariance matrix of $\mathbf{u}$ is

$$\mathbf{Q}(\mathbf{g}) = (\mathbf{g} \otimes \mathbf{g})^{-1} \mathbf{Q} (\mathbf{g} \otimes \mathbf{g})^{-t} \qquad (4)$$

where $\otimes$ denotes the Kronecker product. In this paper, we first define the covariance matrix at the identity $\mathbf{Q}_{\mathbf{I}_{3\times 3}} = q\mathbf{I}_{6\times 6}$, where q is a positive scalar. Further, the covariance matrix at point $\mathbf{X}$ can be computed using (4) by setting $\mathbf{g} = \mathbf{X}^{1/2}$. With this definition, the state transition noise is independent with respect to the system state.

The observation model of our dynamic system is based on (1). The covariance matrix of the observation noise for all the magnetic gradients is denoted by $\mathbf{R}$. Based on the assumptions that the measurements from distinct magnetic gradients are independent, we know that $\mathbf{R}$ is diagonal.

3) Prior Model: For a recursive filter, a prior for the initial state is pretty useful as we need to initialize the filter before the first iteration. Similar to the state transition model, in the prior, we assume the two (random) diffusion tensors are independent and LogNormally distributed, which are very similar to (3). However, since there is no state prior to the initial state, we center the distribution at the diffusion tensors that are estimated at the seed points during the initialization step.

D. The Intrinsic Unscented Kalman Filter

Prediction and correction are the two major stages at each iteration in UKF [31]. In the prediction stage, the state random variable at the current iteration is predicted based on the result of previous steps and the state transition model. In the correction stage, the predicted state is corrected based on the likelihood (observation in the current state together with the observation model) using Bayesian inference. In the fiber tracking problem, the states are on P_n where no vector operations are available, and the observation model in (1) is highly nonlinear. To solve this problem, we propose a nontrivial extension of the UKF, especially for the prediction stage to be valid on P_n.

To begin with, the augmented state for the bi-(diffusion) tensor state at iteration step k is defined as $\mathbf{X}_k = [\mathbf{u}_k^{(1),t}, \mathbf{u}_k^{(2),t}, \mathbf{v}_k^{(1),t}, \mathbf{v}_k^{(2),t}]^t$, where $\mathbf{v}_k^{(i)}$ $i = 1, 2$ is the state transition noise vector for diffusion tensor state $\mathbf{D}_k^{(i)}$ and $\mathbf{u}_k^{(i)} = Log_{E(\mathbf{D}_k^{(i)})}(\mathbf{D}_k^{(i)})$, which is the representation of the state random variable in the tangent plane at its Karcher expectation $(E(\cdot))$. $\mathbf{X}_k$ is zero mean and with covariance matrix denoted by $\mathbf{P}_k^a$. The covariance matrix for the state $[\mathbf{u}_k^{(1),t}, \mathbf{u}_k^{(2),t}]^t$ is denoted by $\mathbf{P}_{k,DD}$. Note that $\mathbf{P}_k^a$ is a block-wise diagonal matrix composed from $\mathbf{P}_{k,DD}$, $\mathbf{Q}_k^{(1)}$, and $\mathbf{Q}_k^{(2)}$, because of the independence of the prior and the state transition noise.

$$\mathbf{P}_k^a = \begin{bmatrix} \mathbf{P}_{k,DD} & 0 & 0 \\ 0 & \mathbf{Q}_k^{(1)} & 0 \\ 0 & 0 & \mathbf{Q}_k^{(2)} \end{bmatrix}. \qquad (5)$$

In the prediction stage, $2L+1$ weighted samples from the distribution of $\mathbf{X}_k^t$ are first computed by a deterministic sampling scheme given below. Here, $L = 24$ and denotes the dimension of $\mathbf{X}_k^t$

$$\mathcal{X}_{k,0} = 0, w_0 = \frac{\kappa}{(L+\kappa)}$$
$$\mathcal{X}_{k,j} = (\sqrt{(L+\kappa)\mathbf{P}_k^a})_j, w_j = \frac{1}{2(L+\kappa)}$$
$$\mathcal{X}_{k,j+L} = -(\sqrt{(L+\kappa)\mathbf{P}_k^a})_j, w_{j+L} = \frac{1}{2(L+\kappa)} \tag{6}$$

where w_j is the weight for the corresponding sample, $\kappa \in R$ is a parameter to control the scatter of the samples, and $(\sqrt{(L+\kappa)\mathbf{P}_k^a})_j$ is the jth column vector of matrix $\sqrt{(L+\kappa)\mathbf{P}_k^a}$.

Since samples $\mathcal{X}_{k,j} = [\mathbf{u}_{k,j}^{(1),t}, \mathbf{u}_{k,j}^{(2),t}, \mathbf{v}_{k,j}^{(1),t}, \mathbf{v}_{k,j}^{(2),t}]^t$ are generated from the joint distribution of posterior and state transition at frame k, we can get the samples from the distribution of prediction in frame $k+1$ based on $\mathcal{X}_{k,j}$ through a two-step procedure. First we can get the samples from the posterior from iteration k

$$\mathbf{D}_{k,j}^{(i)} = \mathrm{Exp}_{\hat{\mathbf{D}}_k^{(i)}}(\mathbf{u}_{k,j}^{(i)}) \tag{7}$$

where $\hat{\mathbf{D}}_k^{(i)}$ is the state estimate from iteration k (the estimator of $E(\mathbf{D}_k^{(i)})$). And then the samples from the predicted distribution can be generated based on $\mathbf{D}_{k,j}^{(i)}$ and $\mathbf{v}_{k,j}^{(i)}$

$$\mathcal{D}_{k+1,j}^{(i)} = \mathrm{Exp}_{\mathbf{D}_{k,j}^{(i)}}(\mathbf{v}_{k,j}^{(i)}) \tag{8}$$

where $\mathcal{D}_{k+1,j}^{(i)}$ denotes the jth sample from the distribution of the prediction. The predicted mean could be computed as the weighted Karcher mean, $\hat{\mathcal{D}}_{k+1}^{(i)} = \widehat{\sum}_j w_j \mathcal{D}_{k+1,j}^{(i)}$ for general state transition functions. However, since $\mathbf{P}_k^a$ in (5) is block-wise diagonal, $\sqrt{(L+\kappa)\mathbf{P}_k^a}$ is also block-wise diagonal, which means for each sample $\mathcal{X}_{k,j}$, either $\mathbf{u}_{k,j}^{(i)}$ or $\mathbf{v}_{k,j}^{(i)}$ is zero. Based on the sampling strategy in (6) and the state transition in (3), it is obvious that $\hat{\mathcal{D}}_{k+1}^{(i)} = \hat{\mathbf{D}}_k^{(i)}$, because, we can only have either $\mathbf{u}_k \neq \mathbf{0}$ or $\mathbf{v}_k \neq \mathbf{0}$, but not both. This means, during the state transition map, either (7) or (8) is an identity map. Based on the sigma points generation [see (6)], the sigma points (for a single tensor) are $\mathbf{D}_k$, $\mathrm{Exp}_{\mathbf{D}_k}(\mathbf{u}_k^i)$, $\mathrm{Exp}_{\mathbf{D}_k}(-\mathbf{u}_k^i), \ldots, Exp_{\mathbf{D}_k}(\mathbf{v}_k^i), Exp_{\mathbf{D}_k}(-\mathbf{v}_k^i), \ldots,$ Since each $\mathbf{v}_k^i$ or $\mathbf{u}_k^i$ has a negative counterpart with the same weight, the sum of Log mapped sigma points at $\mathbf{D}_k$ will be zero, which means the Karcher mean (prediction) of the sigma points is equal to the (identity) transformed previous state. Therefore, we do not actually need to compute the Karcher mean at each iteration, which is known to be computationally expensive.

The predicted covariance of the states is computed in the product space $T_{\hat{\mathcal{D}}_{k+1}^{(1)}} P_3 \times T_{\hat{\mathcal{D}}_{k+1}^{(2)}} P_3$ using, $\mathcal{P}_{k+1,\mathbf{DD}} = \sum_j w_j \mathcal{U}_j \mathcal{U}_j^t$ where

$$\mathcal{U}_j^t = [\mathrm{Log}_{\hat{\mathcal{D}}_{k+1}^{(1)}}(\mathcal{D}_{k+1,j}^{(1)}), \mathrm{Log}_{\hat{\mathcal{D}}_{k+1}^{(2)}}(\mathcal{D}_{k+1,j}^{(2)})]$$

is a concatenation of the two vectors obtained from the Log-map of each predicted sample.

Applying the observation model defined in (1) to the predicted state samples we get the predicted vector of MR signals for different magnetic gradients denoted by $\mathcal{S}_{k+1,j}$. Because this is in a vector space, we can use standard vector operations to compute the predicted mean $\hat{\mathcal{S}}_{k+1}$ as the average of $\mathcal{S}_{k+1,j}$. Using the observation noise covariance $\mathbf{R}$, the predicted observation covariance can be computed as

$$\mathcal{P}_{k+1,\mathbf{SS}} = \mathbf{R} + \sum_j w_j(\mathcal{S}_{k+1,j} - \hat{\mathcal{S}}_{k+1})(\mathcal{S}_{k+1,j} - \hat{\mathcal{S}}_{k+1})^t. \tag{9}$$

Also the cross-correlation matrix between the observation and the states is given by $\mathcal{P}_{k+1,\mathbf{DS}} = \sum_j w_j(\mathcal{U}_j(\mathcal{S}_{k+1,j} - \hat{\mathcal{S}}_{k+1})^t)$.

In the update step, the Kalman gain is computed as $\mathcal{K}_{k+1} = \mathcal{P}_{k+1,\mathbf{DS}} \mathcal{P}_{k+1,\mathbf{SS}}^{-1}$. Knowing the Kalman gain we can update the states and covariance which are given by

$$\hat{\mathbf{D}}_{k+1}^{(i)} = \mathrm{Exp}_{\hat{\mathcal{D}}_{k+1}^{(i)}} \mathbf{z}_{k+1}^{(i)}$$
$$\mathbf{P}_{k+1,DD} = \mathcal{P}_{k+1,\mathbf{DD}} - \mathcal{K}_{k+1} \mathcal{P}_{k,\mathbf{SS}} \mathcal{K}_{k+1}^t \tag{10}$$

where $[\mathbf{z}_{k+1}^{(1),t}, \mathbf{z}_{k+1}^{(2),t}]^t = \mathcal{K}_{k+1}(\mathbf{S}_{k+1} - \hat{\mathcal{S}}_{k+1})$, and $\mathbf{S}_{k+1}$ is the observation (MR signal vector) at step $k+1$.

E. The Tracking Algorithm

The IUKF proposed in Section II-D is a recursive bi-tensor reconstruction algorithm, which can be used to recursively estimate the fiber directions. Combining IUKF with line integration, we can get a fiber tracking algorithm which can track fibers directly from DWMR signals. At iteration k, we can estimate the two tensors $\hat{\mathbf{D}}_k^{(1)}$ and $\hat{\mathbf{D}}_k^{(2)}$ using IUKF described earlier, and their respective principal eigenvectors $\mathbf{v}_k^{(1)}$ and $\mathbf{v}_k^{(2)}$ as candidates. After selecting the direction $\mathbf{v}_k$ from the candidates via comparison to the direction $\mathbf{v}_{k-1}$ from the last iteration, we can propagate the fiber based on the line integral equation, $\mathbf{p}_{k+1} = \mathbf{p}_k + \delta \mathbf{v}_k$, where $\mathbf{p}_k$ is the current point on the fiber at iteration k, and δ is the preselected step size. The stopping criteria in this paper is defined by: 1) if the tract has reached a known boundary, i.e., boundary of the segment or image or, 2) if both candidate directions are far from the previous direction (greater than 60°). To initialize the tracking, a seed region is selected, and a second-order tensor is estimated at each seed point to provide the initial values for IUKF. More details of the initialization process are described in Section III. Finally, in order to perform the multitensor reconstruction in subvoxels along fiber tracts, the DWMR signal is interpolated. Among different interpolation alternatives suited for this framework, e.g., spline, tricubic, etc., we picked the trilinear interpolation technique for simplicity and computational speed.

III. Experiments

In this section, we present extensive validation of our IUKF algorithm for tractography. We present three different experiments to this end. In the first experiment, we evaluate the performance of our IUKF-based tractography algorithm on the data provided at the fibercup challenge competition held in conjunction with the MICCAI'09 [39] and publicly available now on the web. We present comparisons between the performance of our IUKF and three other methods that were judged the top three at this competition. To the best of our knowledge, there are no other published results bettering these methods in terms of performance on the fiber cup data sets. In the second experiment,

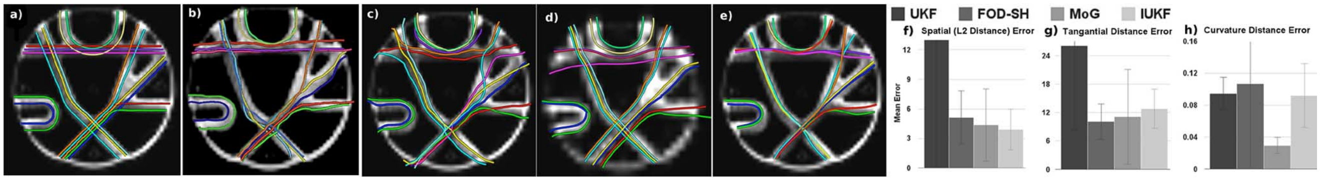

Fig. 1. (I) Tractography results obtained from various algorithms applied to fiber cup phantom data [39]. (a) Ground-truth. (b) IUKF (our method). (c) UKF [31]. (d) FOD-SH [28]. (e) MoG [42]. Images (a), (c), (d), and (e) are reproduced from [39]. (II) Quantitative comparisons between IUKF and the winners of the fiber cup challenge.

we present results of IUKF tractography applied to DWMR data from cervical region of rat spinal cords. We present statistically significant differences between control and injured cords using fiber density maps extracted from estimated tracts. In the final experiment, we applied IUKF tractography to human brain DWMR scans provided during the tractography challenge competition held in conjunction with the MICCAI'12 [41].

A. Results on Fiber cup Phantom Data

We present tractography results from an application of IUKF to the fiber cup phantom data [39], along with the qualitative and quantitative comparisons to three different tractography algorithms [28], [31], [42], which were the declared winners of the challenge. The phantom simulates a coronal section of the human brain, which includes different crossing and kissing fiber bundles with different curvatures. Diffusion MR data was acquired on the 3-T Tim Trio MRI systems of the NeuroSpin Centre, with $b = 1500\ \mathrm{s/mm}^2$ and $\mathrm{voxel\ size} = 3 \times 3 \times 3\ \mathrm{mm}^3$ along 130 diffusion directions. Fig. 1(a)–(e) depicts the fiber tracts obtained using (our method) IUKF, as well as the other three aforementioned algorithms and the ground-truth.

For quantitative validation, we computed the spatial, angular and curvature distances (that were used in the fiber cup competition and are described in [39]) between the fibers estimated by each method and the ground-truth. Fig. 1(f)–(h) illustrates the mean error for the aforementioned measures, computed from our method compared to the first [42], second [28], and third [31] ranked winners of fiber cup challenge, which are labeled as MOG, FOD, and UKF, respectively. The mean spatial distance errors for IUKF, MOG, FOD, and UKF are 3.91, 4.35, 5.13, and 12.98, respectively. It is evident that IUKF outperforms all of the winners of the fiber cup challenge with respect to the spatial distance error measure.

Moreover, the mean error using angular distance for IUKF, MOG, FOD, and UKF are, respectively, 12.80, 11.07, 10.08, and 26.11. Using the curvature distance, the mean errors are 0.091, 0.029, 0.106, and 0.094, respectively. Note that in these error measures IUKF is still competitive when compared to the winners of the fiber cup challenge. Specifically, it should be noted that with regards to all the three error measures, IUKF performs better than the nonintrinsic recursive filter based approach in [31], one which was ranked third in the fiber cup challenge. Further, the standard deviations of all the three error measures for the four methods were: (a) Spatial error: UKF (19.29), FOD-SH (2.71), MoG (3.67), IUKF (2.08); (b) Tangential error: UKF (17.81), FOD-SH (3.73), MoG (10.02), IUKF (4.16); (c) Curvature error: UKF (0.02), FOD-SH (0.2), MoG (0.01), IUKF (0.04). Note that IUKF provides reasonably small standard deviations with respect to all the three error measures compared to the competing methods. Also, our tractography algorithm does not require extensive tuning of parameters in achieving the results shown here.

B. Spinal Cord Tractography

In this section we describe the application of our tractography technique to detect spinal cord injuries. In this study, we performed tractography on HARDI scans of rat cervical spinal cord at $C3-C5$. The group contained seven different scans including five control and two injured rats with injury in the thoracic spinal cord.

The HARDI scan for each rat was acquired using a 17.6-T Brucker scanner, along 21 directions with a b value of $1000\ \mathrm{s/mm}^2$ along with a single image acquired at b value close to zero. Echo time and repetition time were $21.174\ \mathrm{ms}$ and $3.5\ \mathrm{s}$, respectively; Δ and δ values were $13.4\ \mathrm{ms}$ and $1.8\ \mathrm{ms}$; the voxel size of the scan was $35\ \mu\mathrm{m} \times 35\ \mu\mathrm{m} \times 300\ \mu\mathrm{m}$; and the image resolution was 128×128 in the $x - y$ plane, and 22 to 26 in the z-direction.

First, the fiber bundles in each dataset are tracked using the IUKF algorithm and for comparison, we used the Constrained Spherical Deconvolution (CSD) algorithm proposed in [28] and implemented as part of MRtrix-0.2.11 software [43]. Moreover, to illustrate the differences between the IUKF and UKF, we also applied the published UKF code which is available at http://www.nitrc.org/projects/ukftractography. To initialize each of the tractography algorithms, seed points were placed over the entire grey matter. In IUKF, a bitensor model estimation was employed at each seed point to initialize the algorithm. Also, we set the state transition noise variance in (3), $\mathbf{Q}_1 = \mathbf{Q}_2 = 0.08\mathbf{I}$, the observation noise variance $\mathbf{R} = 0.003I$ and the size of each tracking step $\delta t = 0.01\ \mathrm{mm}$. Although, there are systematic ways to estimate the observation noise variance $\mathbf{R}$ [44] and the state transition noise variance, $\mathbf{Q}_i$ from the data, in this paper, we empirically found values that were quite robust in all our experiments.

Based on the type of injury (contusion) in the thoracic spinal cord, we were particularly interested in the motoneuron fiber bundle, which emanates from the grey matter and continues almost horizontally to the boundary of the spinal cord. Therefore, to remove the "unwanted" fibers we applied the following angle threshold criteria to each tractography result: any fiber with an angle less than 10° with the z axis is discarded. This way the fiber bundles which are passing vertically through all slices are removed, and the ones that are sufficiently horizontal

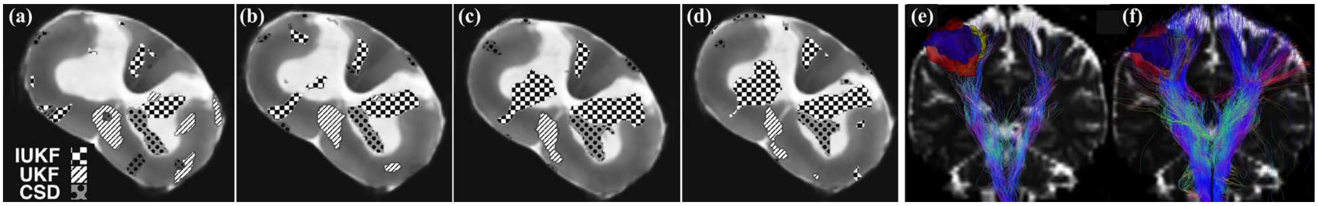

Fig. 2. (I) T-test analysis on fiber densities for IUKF (squares), UKF (hatched) and CSD (dots). Images (a), (b), (c), and (d) illustrate the regions in slices 8, 9, 10, and 11, respectively, with p-value less than 0.05, overlaid on the atlas S_0 image. (II) Coronal view of the tractography results using UKF (e) and IUKF (f) on the human brain dataset.

survived. We applied the same angle threshold to the results of each method on each dataset.

The differences between the fiber tracts from injured and control rats cannot be visually discerned directly from the bundles. To visualize the differences, axonal fiber density maps are computed for each data set by counting the number of fibers passing through a 3×3 neighborhood of each voxel. In order to perform a voxelwise comparison between the axonal densities from the injured and control spinal cords, the density maps then were deformed nonlinearly to a spinal cord atlas derived from the HARDI data using the method described in [45]. Finally, a voxelwise t-test analysis was employed, and the regions with the p-value less than 0.05 were extracted to highlight the areas with significant differences.

Fig. 2(a)–(d) illustrates the regions obtained from tractography using IUKF, UKF, and CSD, represented using squares, hatches and dots, respectively and overlaid on the spinal cord atlas S_0 image (zero magnetic field gradient image). It can be seen that the IUKF results indicate significant differences between the control and injured subjects, in the motoneuron regions, while CSD and UKF were not able to discriminate between normal and injured datasets in these regions when compared to the IUKF. This experiment shows the effectiveness of the fiber density maps computed using our tractography method, as a biomarker to detect spinal cord injuries.

C. *Human Brain Tractography*

In this section we present the results of our tractography algorithm on human brain datasets. The patient human brain scan was acquired for the tractography challenge at MICCAI'12 using a 3.0-T EXCITE Signa scanner with 31 gradient directions and 1 baseline was used. The acquisition parameters were as follows: $b = 1000\ \mathrm{s/mm}^2$, $\mathrm{TR} = 14000\ \mathrm{ms}$, $\mathrm{TE} = 30\ \mathrm{ms}$, $\mathrm{FOV} = 25.6\ \mathrm{cm}$. Whole brain coverage was obtained by collecting 52 slices with $1.0\ \mathrm{mm} \times 1.0\ \mathrm{mm}$ voxel size and $2.6\ \mathrm{mm}$ slice thickness [41].

In this experiment, we tracked the corticospinal tract which starts in the cerebral cortex and terminates in the spinal cord. To reconstruct these fibers, we first performed a full brain IUKF tractography, by placing seed points in every voxels inside the brain. For the sake of comparison, we also performed tractography using the publicly available UKF code [31]. The input dataset and the seeding regions in both UKF and IUKF were exactly the same. Then two fiber reduction criteria were applied to discard "unwanted" fibers from each method.

Firsty, each retained fiber must pass through both ROIs, one at the top of the brain, and the other in the brainstem. In this way, the fiber length criterion is implicitly applied, such that only fibers that are long enough to start from the brain stem and end in the cortex are retained.

Second, based on the structure of corticospinal tracts, the fibers with an angle less than 60° to the axial plane are removed from results. Fig. 2(e) and (f) illustrates the coronal view of the resulting fibers from each method in the presence of a tumor. It can be seen that starting from the stem, tracts obtained from IUKF reach multiple regions of motor cortex, as expected. Further, as anticipated it can be observed that there is a good number of tracts reconstructed by IUKF in both the healthy and the pathological sides, while UKF was not able to detect as many corticospinal tracts as IUKF.

IV. Conclusion

We have presented a novel intrinsic unscented Kalman filter (IUKF) to achieve simultaneous estimation of multitensors and tractography. The key difference between the existing unscented Kalman filter algorithm for tractography and the method presented here is the theory and implementation of our technique which makes use of the group operations on the manifold of diffusion tensors, a Riemannian manifold and not a vector space and hence vector space operations if used can result in erroneous predictions. We tested the algorithm on several data sets including the fibercup challenge data [39], rat spinal cords with and without injury and human brain data sets from the tractography challenge held in conjunction with MICCAI'12. For the experiments on rat spinal cords, we also depicted the differences between the tracts in cords with and without injury and quantified them via the axonal density measure. In all our comparisons, the IUKF algorithm performed either better than the state-of-the-art or was quite competitive.

Acknowledgment

The authors would like to thank Dr. Howland and Dr. M. S. Hwang for providing the Spinal Cord HARDI datasets.

References

[1] P. Basser *et al.*, "*In vivo* fiber tractography using DT-MRI data," *Magn. Reson. Med.*, vol. 44, pp. 625–632, 2000.
[2] T. E. Conturo *et al.*, "Tracking neuronal fiber pathways in the living human brain," *Proc. Nat. Acad. Sci.*, vol. 96, no. 18, pp. 10422–10427, 1999.
[3] B. C. Vemuri *et al.*, "Fiber tract mapping from diffusion tensor MRI," in *Proc. IEEE Workshop VLSM*, 2001, pp. 81–88.
[4] T. McGraw *et al.*, "DT-MRI denoising and neuronal fiber tracking," *Med. Imag. Anal.*, vol. 8, pp. 95–111, 2004.
[5] B. Jian *et al.*, "A novel tensor distribution model for the diffusion-weighted MR signal," *NeuroImage*, vol. 37, no. 1, pp. 164–176, 2007.

[6] A. Barmpoutis *et al.*, "Extracting tractosemas from a displacement probability field for tractography in DW-MRI," in *MICCAI*. New York: Springer, 2008, pp. 9–16.
[7] C. Gössl *et al.*, "Fiber tracking from DTI using linear state space models: Detectability of the pyramidal tract," *NeuroImage*, vol. 16, no. 2, pp. 378–388, 2002.
[8] M. Lazar *et al.*, "White matter tractography using diffusion tensor deflection," *Human Brain Map.*, vol. 18, no. 4, pp. 306–321, 2003.
[9] E. Özarslan and T. H. Mareci, "Generalized diffusion tensor imaging and analytical relationships between diffusion tensor imaging and high angular resolution diffusion imaging," *Magn. Reson. Med.*, vol. 50, pp. 955–965, 2003.
[10] C. Liu *et al.*, "Characterizing non-Gaussian diffusion by using generalized diffusion tensors," *Magn. Reson. Med.*, vol. 51, no. 5, pp. 924–937, 2004.
[11] A. Barmpoutis *et al.*, "Regularized positive-definite fourth order tensor field estimation from DW-MRI," *NeuroImage*, vol. 45, no. 1, pp. S153–S162, 2009.
[12] A. Ghosh *et al.*, "A polynomial based approach to extract fiber directions from the ODF and its experimental validation," *Magn. Reson. Med.*, 2009.
[13] E. Özarslan *et al.*, "Resolution of complex tissue micro-architecture using the diffusion orientation transform," *NeuroImage*, vol. 31, pp. 1086–1103, 2006.
[14] P. Hagmann *et al.*, "Diffusion spectrum imaging tractography in complex cerebral white matter: An investigation of the centrum semiovale," *Magn. Reson. Med.*, vol. 52, 2004.
[15] J. Cheng *et al.*, "A Riemannian framework for orientation distribution function computing," in *MICCAI*. New York: Springer, 2009, pp. 911–918.
[16] A. A. Qazi *et al.*, "Resolving crossings in the corticospinal tract by two-tensor streamline tractography: Method and clinical assessment using fMRI," *NeuroImage*, vol. 47, pp. T98–T106, 2009.
[17] D. S. Tuch, "Q-ball imaging," *Magn. Reson. Med.*, vol. 52, no. 6, pp. 1358–1372, 2004.
[18] X. Hao *et al.*, "Adaptive Riemannian metrics for improved geodesic tracking of white matter," in *IPMI*. New York: Springer, 2011, pp. 13–24.
[19] L. O'Donnell *et al.*, "New approaches to estimation of white matter connectivity in diffusion tensor MRI: Elliptic pdes and geodesics in a tensor-warped space," in *MICCAI*. New York: Springer, 2002, pp. 459–466.
[20] T. Behrens *et al.*, "Characterization and propagation of uncertainty in diffusion-weighted MR imaging," *Magn. Reson. Med.*, vol. 50, no. 5, pp. 1077–1088, 2003.
[21] M. Björnemo *et al.*, "Regularized stochastic white matter tractography using diffusion tensor MRI," in *MICCAI*. : Springer, 2002, pp. 435–442.
[22] T. Behrens *et al.*, "Probabilistic diffusion tractography with multiple fibre orientations: What can we gain?," *NeuroImage*, vol. 34, no. 1, pp. 144–155, 2007.
[23] G. Parker and D. Alexander, "Probabilistic Monte Carlo based mapping of cerebral connections utilising whole-brain crossing fibre information," in *IPMI*. New York: Springer, 2003, pp. 684–695.
[24] I. Aganj *et al.*, "A hough transform global probabilistic approach to multiple-subject diffusion MRI tractography," *Med. Imag. Anal.*, vol. 15, no. 4, pp. 414–425, 2011.
[25] D. K. Jones, "Tractography gone wild: probabilistic fibre tracking using the wild bootstrap with diffusion tensor MRI," *IEEE Trans. Med. Imag.*, vol. 27, no. 9, pp. 1268–1274, Sep. 2008.
[26] B. Yoldemir *et al.*, "SMT: A reliability based interactive DTI tractography algorithm," *IEEE Trans. Med. Imag.*, vol. 31, no. 10, pp. 1929–1940, Oct. 2012.
[27] J. I. Berman *et al.*, "Probabilistic streamline q-ball tractography using the residual bootstrap," *NeuroImage*, vol. 39, no. 1, pp. 215–222, 2008.
[28] B. Jeurissen *et al.*, "Probabilistic fiber tracking using the residual bootstrap with constrained spherical deconvolution," *Human Brain Map.*, vol. 32, no. 3, pp. 461–479, 2011.
[29] P. MomayyezSiahkal *et al.*, "Beyond crossing fibres: Probabilistic tractography of complex subvoxel fibre geometries," in *Proc. MICCAI Workshop DMFC*, 2009, pp. 81–92.
[30] M. Descoteaux *et al.*, "Deterministic and probabilistic tractography based on complex fibre orientation distributions," *IEEE Trans. Med. Imag.*, vol. 28, no. 2, pp. 269–286, Feb. 2009.
[31] J. G. Malcolm *et al.*, "Filtered multi-tensor tractography," *IEEE Trans. Med. Imag.*, vol. 29, no. 9, pp. 1664–1675, Sep. 2010.
[32] S. J. Julier and J. K. Uhlmann, "Unscented filtering and nonlinear estimation," *Proc. IEEE*, vol. 92, no. 3, pp. 401–422, Mar. 2004.
[33] S. Lienhard *et al.*, "A full bi-tensor neural tractography algorithm using the unscented Kalman filter," *J. EURASIP*, vol. 2011, no. 1, pp. 1–10, 2011.
[34] H.E. Cetingul *et al.*, "Simultaneous ODF estimation and tractography in HARDI," in *Proc. IEEE Eng. Med. Biol. Soc. Conf.*, 2012, pp. 86–89.
[35] J. G. Malcolm *et al.*, "A filtered approach to neural tractography using the Watson directional function," *Med. Imag. Anal.*, vol. 14, no. 1, p. 58, 2010.
[36] S. Helgason, *Differential Geometry, Lie Groups, and Symmetric Spaces*. New York: Academic, 2001.
[37] S. Hauberg *et al.*, "Unscented Kalman filtering on Riemannian manifolds," *J. Math. Imag. Vis.*, pp. 1–18, 2013.
[38] G. Cheng *et al.*, "A novel intrinsic unscented Kalman filter for tractography from HARDI," in *Proc. IEEE Int. Symp. Biomed. Imag.*, 2012, pp. 534–537.
[39] P. Fillard *et al.*, "Quantitative evaluation of 10 tractography algorithms on a realistic diffusion MR phantom," *NeuroImage*, vol. 56, no. 1, pp. 220–234, 2011.
[40] A. Schwartzman, "Random ellipsoids and false discovery rates: Statistics for diffusion tensor imaging data," Ph.D. dissertation, Stanford Univ., Stanford, CA, 2006.
[41] S. Pujol *et al.*, "Miccai DTI tractography challenge—2nd edition," in *Proc. MICCAI*, Nice, France, 2012.
[42] M. Reisert *et al.*, "Tracking a physical phantom by global fibre reconstruction," in *MICCAI Workshop DMFC*, London, U.K., 2009, pp. 70–82.
[43] J. D. Tournier *et al.*, "MRtrix: Diffusion tractography in crossing fiber regions," *Int. J. Imag. Syst. Tech.*, vol. 22, no. 1, pp. 53–66, 2012.
[44] Z. Wang *et al.*, "A constrained variational principle for direct estimation and smoothing of the diffusion tensor field from complex DWI," *IEEE Trans. Med. Imag.*, vol. 23, no. 8, pp. 930–939, Aug. 2004.
[45] G. Cheng *et al.*, "Atlas construction for high angular resolution diffusion imaging data represented by Gaussian mixture fields," in *Proc. Int. Symp. Biomed. Imag.*, 2011, pp. 549–552.